Seventh International Conference on
Computational Fluid Dynamics (ICCFD7),
Big Island, Hawaii, July 9-13, 2012

ICCFD7-2601

Numerical Simulation of Incompressible Viscous Flow using a Velocity-Pressure-Vorticity Variational Formulation and Direct Solver

Ben Chacón and Mohamed Hafez
University of California, Davis
Corresponding author: bchacon@ucdavis.edu

Abstract: The two-dimensional incompressible viscous flow equations are solved by iterating on the kinematics, pressure and momentum equations producing a solution that satisfies source and vorticity definitions up to machine accuracy. Given a vorticity and mass fields, a functional is constructed to measure the kinematic imbalance of a velocity field. The velocity equations are produced by minimizing a discrete functional, subject to constrains imposed by boundary conditions. A suitable preconditioning and interpolation technique are used to balance precision and computation speed. The Poisson equation for pressure is solved similarly by minimizing a suitable functional. The momentum equations are then solved using a finite volume approach. A controlled amount of artificial viscosity is added according to mesh size and Reynolds number, resulting in a stable calculation implemented using a direct solver.

Keywords: Numerical Algorithms, Computational Fluid Dynamics, Vorticity, Discrete Functional, Minimization.

1. Introduction

Classically, formulations of the incompressible Navier-Stokes equations using a scalar stream function and vorticity are computationally attractive and conserve mass automatically but generalization to three dimensional flows are nontrivial [1]. Other techniques like velocity-vorticity formulations aim to simplify the gap between two and three dimensions, but they impose mass conservation explicitly as an extra equation. New challenges arise with these techniques, such as checkerboard decoupling of the velocity equations and complications in multiply-connected domains [2], [3], [4]. Velocity-pressure methods have proven practical as in [5], but they rely on a pressure and velocity correction. Moreover, most incompressible flow solvers do not guarantee that mass and vorticity definitions are preserved in the discrete sense. Consequently, their solutions are corrupted by small amounts of mass and vorticity generated in the flow field.

The present work develops a new approach using a velocity-pressure-vorticity formulation. A Poisson equation for pressure is solved, so no pressure/velocity relation or artificial compressibility is necessary. Further techniques deal with artificial velocity decoupling and to accelerate convergence, leading to a one-parameter family of schemes that balance decoupling precision and convergence

speed depending on the geometry. Similarly, the vorticity is obtained from the curl of the velocity, which is obtained from the momentum equation. Proper up-winding can be tuned to achieve stability. The technique is presented for steady two dimensional flows, but it can be generalized to unsteady three-dimensional and compressible flows.

2. Formulation

Separate formulations are constructed for the kinematics, pressure and momentum equations. After discretization, a solution method is implemented alternating velocity, pressure and vorticity iterations in a segregated manner. On every iteration, each separate solution field is solved independently using the PARDISO direct solver (see [6], [7] and [8]), taking advantage of its parallelization, memory efficiency and Bunch-Kaufmann pivoting. Matrix coefficients are stored using the sparse Yale format. The only limitation on the size of the problem is given by memory constraints.

The kinematics and pressure equations are linear and their coefficient matrices depend only on the grid. For them, most of the solution process can be pre-computed resulting in a very time-efficient formulation. The right-hand-side of these equations is also efficiently implemented using vectorization.

On the other hand, for the momentum equation the PARDISO pre-process step optimizes the solution order based on the structure of the coefficient matrix. In order to reduce compute time, advection and diffusion terms are computed in parallel using OpenMP.

The three sets of equations to be solved are described below.

2.1 Kinematics Equations

In the differential level, given a fixed source s and vorticity $\boldsymbol{\omega}$ fields on a volume Ω, the kinematic velocity field $\boldsymbol{V}$ must satisfy the mass and vorticity relations;
$$\nabla \cdot \boldsymbol{V} = s, \qquad \nabla \times \boldsymbol{V} = \boldsymbol{\omega}.$$
The classical solution of this problem is obtained using calculus of variations, by minimizing the functional

$$E = \iint_{\Omega} (\nabla \cdot \boldsymbol{V} - s)^2 + \|\nabla \times \boldsymbol{V} - \boldsymbol{\omega}\|^2 dA,$$

In the discrete context of a computational grid, analogous conditions are imposed. The velocities are defined at the nodes of the grid. The derivatives are computed as line integrals on the polygonal boundary of each cell (Gauss theorem) and the mass and vorticity fields are defined as values on each cell of the grid.

The differential solution method is completely reproduced at the discrete level. The discrete functional takes the form

$$E = \sum_{k} (\nabla_k \cdot \boldsymbol{V} - s_k)^2 + \|\nabla_k \times \boldsymbol{V} - \boldsymbol{\omega}_k\|^2,$$

where the summation ranges over all grid cells. In the present work s_k vanishes identically. Further analysis shows that the discrete terms must be preconditioned by the inverse of a discrete cell area in order for it to yield a correct Laplace formula. Moreover, checkerboard decoupling is avoided by introducing a one-parameter family of discrete radial interpolation schemes that balances decoupling precision and convergence speed [9]. The kinematic equations are finally obtained through a Lagrange multipliers technique minimizing the discrete functional with respect to the velocity values, constrained by suitable boundary conditions.

2.2 Pressure Equations

Given a velocity field V, a quadratic functional is built to measure the pressure imbalance;

$$F = \iint_{\Omega} \|\nabla P - f\|^2 dA,$$

where the vector term f is obtained from the momentum equation (as discussed below) and simplified using the mass conservation equation. Numerically, the term f is evaluated based on the velocity field obtained from the solution of the kinematics equation.

This process is again reproduced in the discrete level, where the pressure values are given at the cell centers and derivatives are similarly computed as line integrals along the boundary of dual cells (around each node). The lack of physical boundary conditions on the pressure equation arises naturally. The fact that there are no pressure variables located at the boundary of the physical domain Ω is a consequence of dual grid nature of the pressure computation.

Preconditioning and radial interpolation schemes are again implemented to improve performance. Algebraic minimization yields the discrete Poisson pressure equation.

2.3 Momentum Equations

Given an advection velocity field V and a pressure field P, the vorticity equation is typically obtained by taking the curl of the vector form of the momentum equation;

$$\nabla \cdot (V \otimes \overline{V}) = -\nabla P + \frac{1}{\text{Re}} \nabla^2 \overline{V}.$$

However, such techniques may compromise the robustness of the solution, especially in terms of its dependence on the boundary geometry. For that reason, the full momentum equation is instead discretized using a direct finite volume technique and solved for the velocity $\overline{V}$. Furthermore, proper up-winding is applied to guarantee stability of the calculations. The vorticity is computed a posteriori from the velocity field obtained from the solution of the momentum equation.

3. Numerical Results

All cases presented here have no sources in the field ($s = 0$). The results below show incompressible external flow solutions around a solid body. All simulations were performed on a desktop pc with an Intel Xeon CPU (2.67 GHz). The results can be divided in five categories: inviscid cylinder, inviscid airfoil, viscous cylinder, rotating viscous cylinder and viscous airfoil.

3.1 Inviscid Cylinder

The equations were solved for inviscid flow around a cylinder on a structured O-grid with 160×120 nodes. Thanks to the smoothness of the geometry (constant curvature). This case shows no decoupling, so no interpolation was applied. As the equation to solve is linear and it is solved using a direct solver, all solutions were calculated without the need to iterate, reaching the solution in less than one second in all cases studied.

Multiple boundary conditions were studied including rotating cylinders and cylinders with a boundary flux. It was verified a posteriori that in all cases the error in the mass and vorticity definitions were of the order of round-off error, showing that the method is exact at the discrete level and the accuracy depends only on the grid resolution. As this case has an exact solution, the solution error can be

directly computed. In all cases the relative error was 0.00086%. Velocity contours around a solid fixed cylinder are shown in Figure 1.
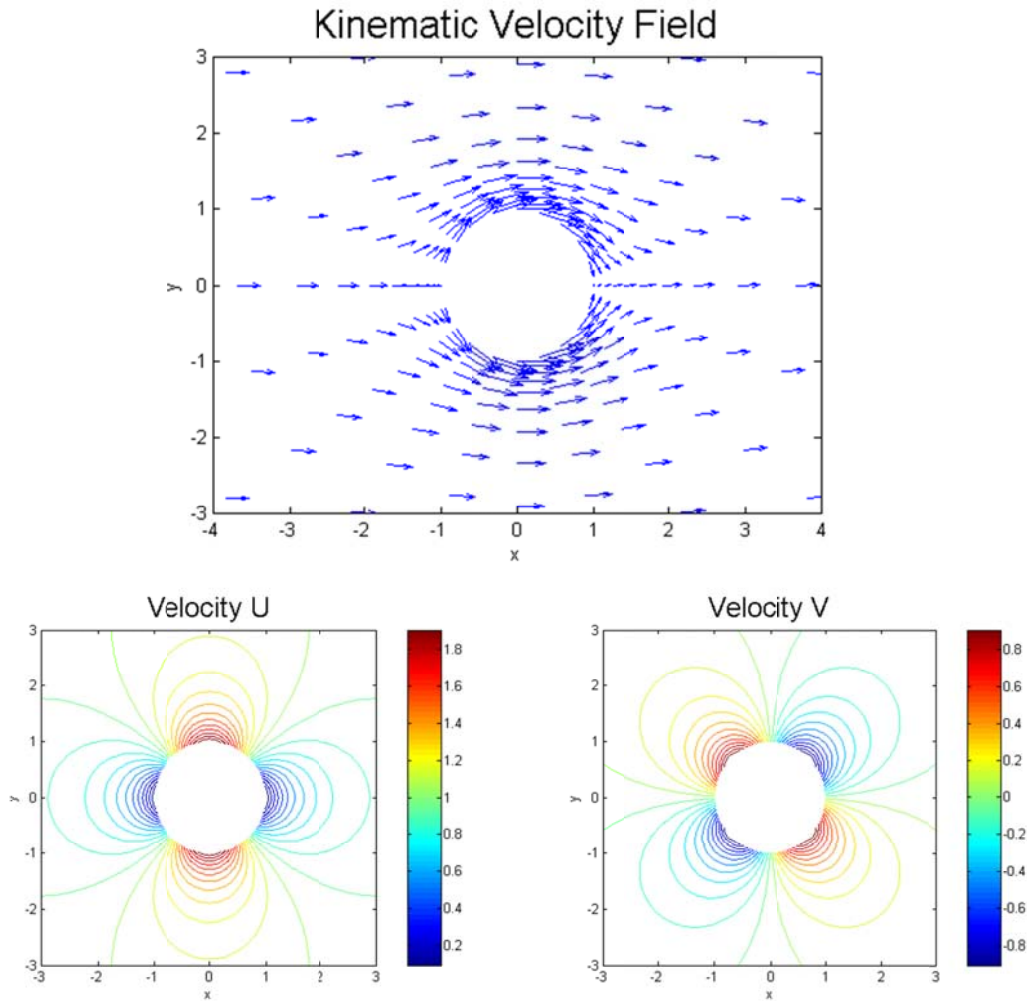

Figure 1. Velocity contours for inviscid flow around a cylinder.

The order of accuracy is studied by analyzing the magnitude of the error on grids of different resolutions. A coarse grid is successively refined. The number of nodes and cells of every successive refinement is shown in Table 1. The maximal error of the solution is seen in Figure 2 . The order of accuracy r of every subsequent grid refinement is obtained from the equation $E_f/E_c = (1/2)^r$, where E_f and E_c are the errors on the fine and coarse grid respectively and the factor $1/2$ is the order of the refinement. Figure 3 shows that the method is in fact second order accurate as predicted by theory.

Grid	Nodes	Cells
1	20×16	20×15
2	40×31	40×30
3	80×61	80×60
4	160×121	160×120
5	320×241	320×240
6	640×481	640×480

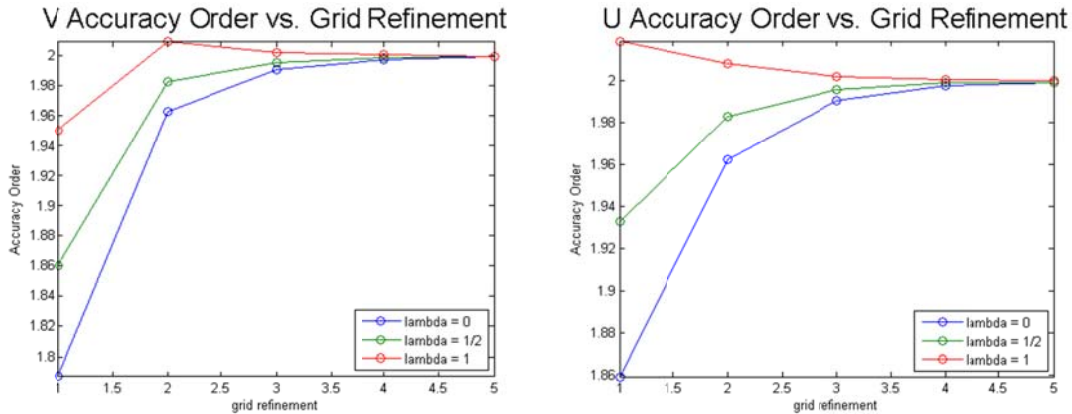**Table 1.** Grid refinements for accuracy analysis.

4

Figure 2. Maximal error for successive grid refinements.
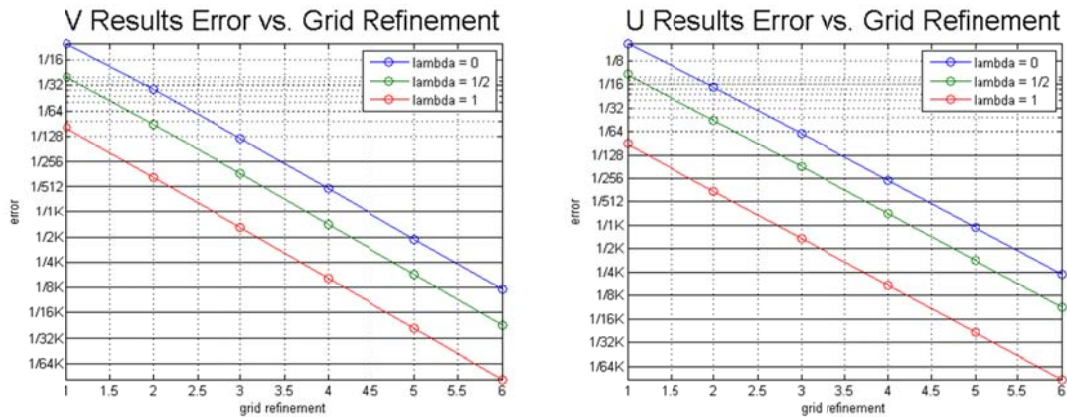

Figure 3. Accuracy order for successive grid refinements.

3.2 Inviscid Airfoil

The solution method is now applied to find the inviscid flow around an airfoil NACA 0012. A structured O-grid of 158×240 nodes was used. Numerically, the solution for inviscid flow around an airfoil shows decoupling originating from the singularity at the trailing edge, so the radial interpolation parameter was reduced to $1/2$, eliminating decoupling at the cost of sacrificing discrete numerical precision. The disturbance introduced in the velocity field by interpolating was small enough to go unnoticed in this study. Moreover, as the method is second order, this disturbance can be further reduced by refining the grid, as shown in the previous section.

Inviscid flows were computed for angles of attack between 0 and 14. Velocity results for an angle of attack of 10 degrees are shown in Figure 4. Pressure profiles were also computed and compared with Xfoil results as presented in Figure 5. The curves produced by both methods are in excellent agreement. Lift was calculated from the pressure and compared to Xfoil values. Results are presented in Table 2. It is seen that the both methods are practically identical and the error remains below 0.1%.
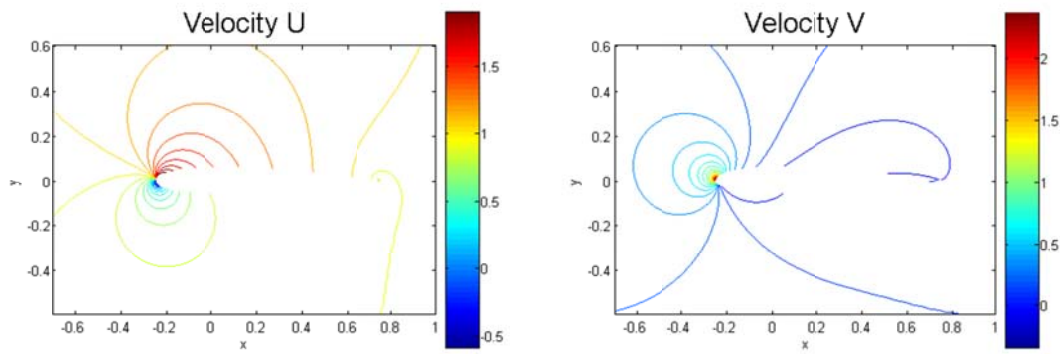
Figure 4. Velocity contours for inviscid flow around an airfoil NACA 0012 at an angle of attack of **10°**.
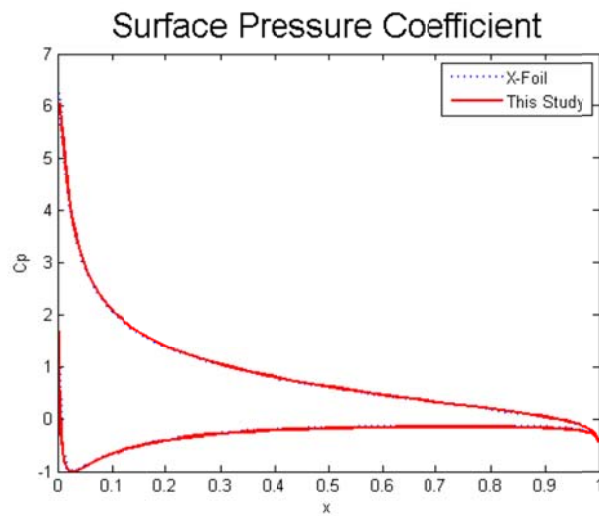

Figure 5. Pressure profile for an inviscid flow around an airfoil NACA 0012 at an angle of attack of **10°**.

α	Circulation	Lift (computed)	Lift (Xfoil)	% Error
2	-0.1207	0.2415	0.2416	0.04
4	-0.2412	0.4826	0.4826	0.06
6	-0.3614	0.7232	0.7236	0.06
8	-0.4812	0.9628	0.9634	0.06
10	-0.6004	1.2012	1.2021	0.07
12	-0.7188	1.4381	1.4393	0.08
14	-0.8364	1.6731	1.6748	0.10

Table 2. Airfoil lift for different angles of attack.

3.3 Viscous Cylinder

Flow around a cylinder was computed for several Reynolds numbers. The equations were solved to machine accuracy on a structured O-grid with 160×120 nodes. Due to the smoothness of the geometry, this case shows no decoupling, so no interpolation was applied. Artificial viscosity was not necessary because the Reynolds numbers were low. Most of the cases were solved in a few dozen iterations, the exception being the computation for $Re = 50$ due to numerical instabilities (the case is on the borderline between steady and unsteady flows). The number of iterations and clock time are presented in Table 3.

Re	Number of Iterations	Clock Time (mm:ss)
10	38	0:09
20	39	0:09
30	55	0:12
40	104	0:21
50	388	1:17

Table 3. Solver performance for flow around a cylinder at several Reynolds numbers.

Results for a Reynolds number of 40 are shown in the figures below. Figure 7 shows the convergence history to machine accuracy. The velocity and vorticity contours are presented in Figure 6. It can be noted that a separation bubble arises behind the cylinder. The size of the separation region and the coefficient of drag for different Reynolds numbers are presented in Figure 8 together with some other numerical [10], [11] and experimental results [12]. The quantities computed show good agreement with the results published in literature.
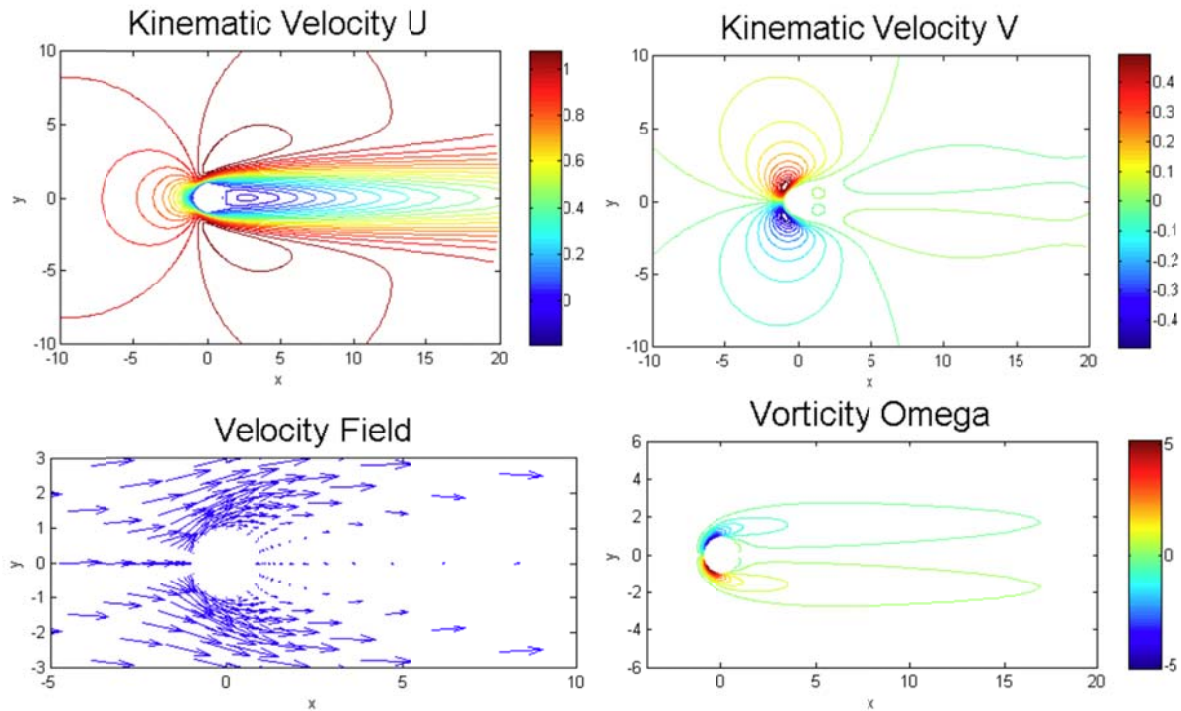

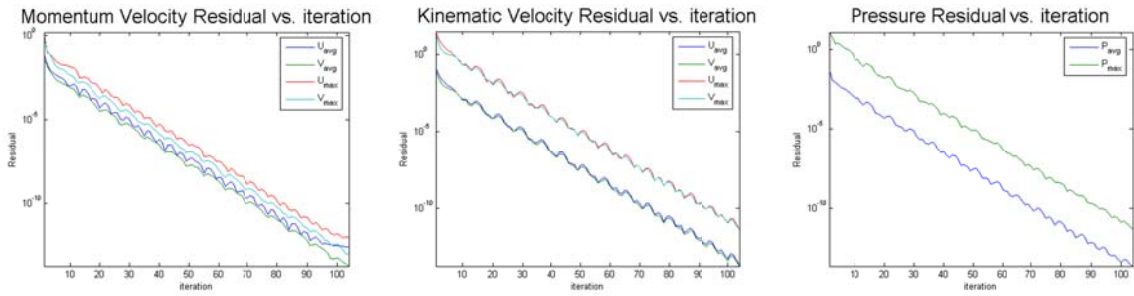**Figure 6.** Velocity and vorticity around a cylinder at $Re = 40$.

Figure 7. Convergence history for viscous flow
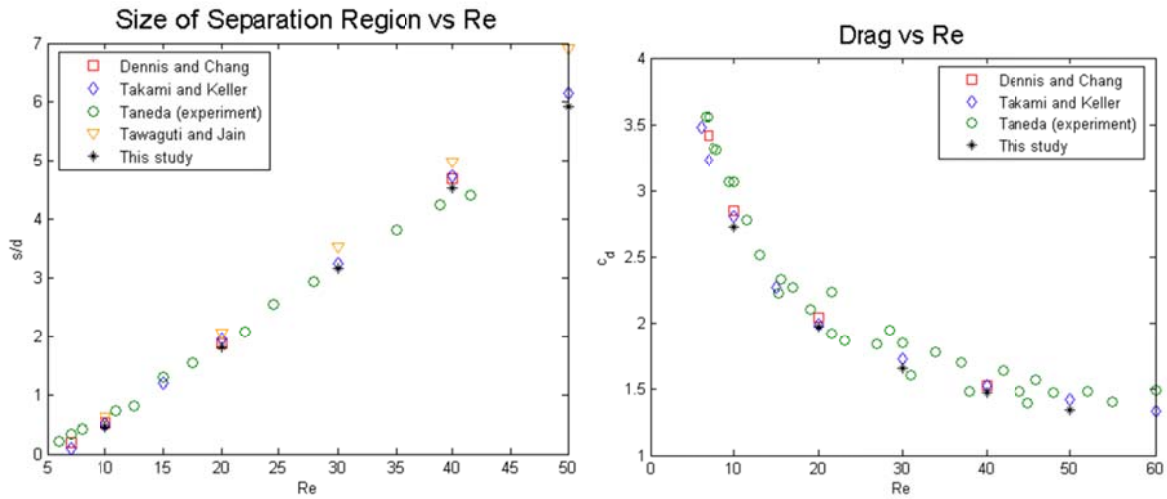around a cylinder at $Re = 40$.

Figure 8. Size of the separation region and coefficient of drag for
a cylinder at several Reynolds numbers.

3.4 Rotating Viscous Cylinder

Using the same grid as the previous case, the flow is now computed over a rotating cylinder at several
Reynolds numbers and rate of rotation, where the non-dimensional rotation rate α is normalized using
the cylinder radius and the velocity of the undisturbed flow. As before, no interpolation or artificial
viscosity is necessary. The performance of the solver is of the same order as the non-rotating cases
presented before.

Several results for Re = 20 are shown in Figure 9 and Figure 10. The dimensionless values for lift and
drag are computed by adding the contributions from pressure and shear stress over the surface of the
cylinder. The values of both forces are in good agreement with references [13] and [14] as shown in
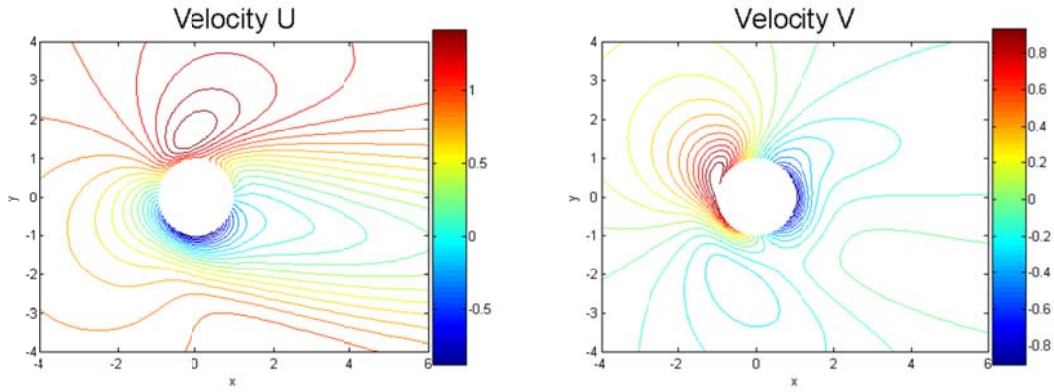Figure 11.

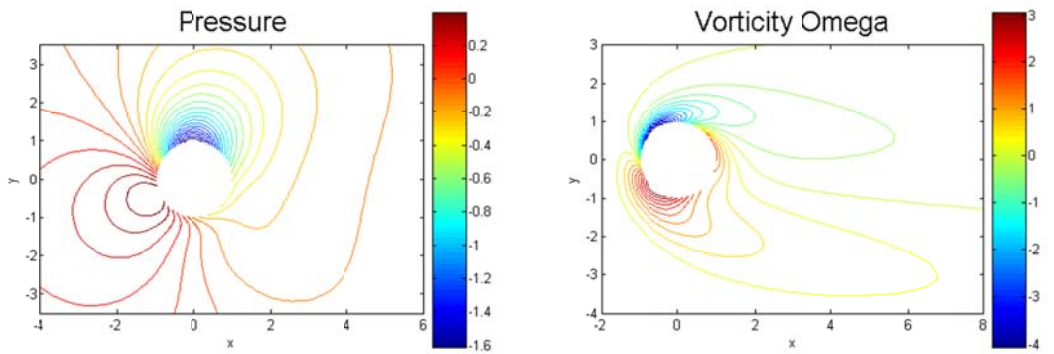**Figure 9.** Velocity contours for a rotating cylinder
at $Re = 20$ and $\alpha = 1$.

Figure 10. Pressure and vorticity contours for a rotating cylinder
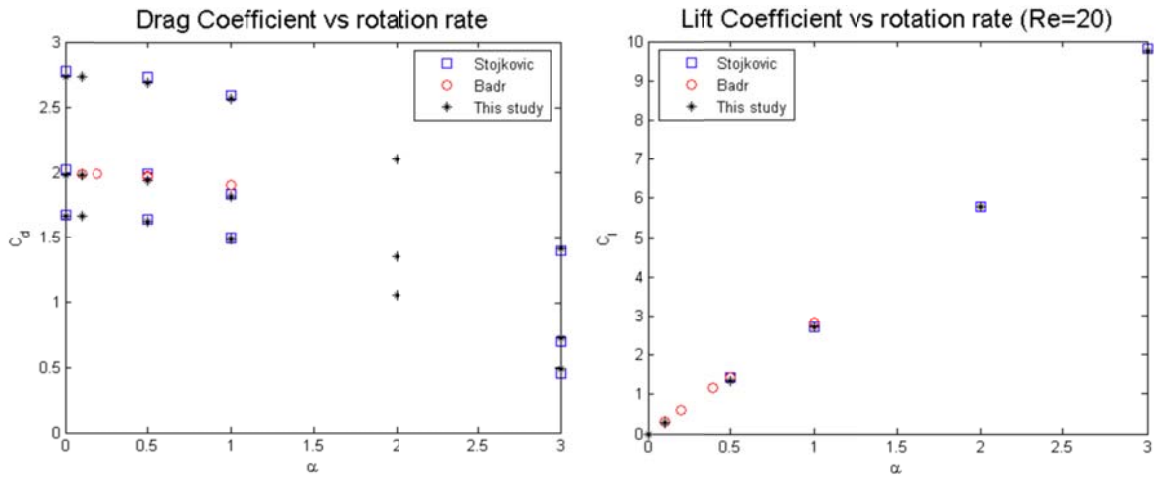at $Re = 20$ and $\alpha = 1$.

Figure 11. Drag coefficient vs. rotation rate for several Reynolds
numbers and lift coefficient vs. rotation rate for $Re = 20$.

3.5 Viscous Airfoil

The solution method is now applied to find the flow around an airfoil NACA 0012 at $Re = 500$. A structured O-grid of 158×240 nodes was used. A preliminary solution shows decoupling in the neighborhood of the sharp trailing edge. Decoupling was eliminated by radial interpolation of the scheme. Another obstacle to overcome was numerical instability produced by the dominant advection terms as a consequence of a higher Reynolds number. Artificial viscosity was introduced to maintain a diagonal dominant system of equations and improve stability and convergence speed.

α	Number of iterations	Clock Time (mm:ss)
0	37	00:27
2	39	00:28
4	42	00:30
6	66	00:46
8	257	02:54
10	1762	17:02

Table 4. Solver performance for flow around an airfoil NACA 0012
at several angles of attack.

The flow was computed for different angles of attack. The number of iterations and clock time are presented in Table 4. For low angles of attack (six or less) the solver converged in a few dozen iterations, taking less than a minute of clock time. For larger angles of attack, numerical stability and non-linearity undermined the solver performance and smaller artificial time steps were required to reach convergence. As a consequence, the solver needed more iterations and time to find a solution to machine accuracy.
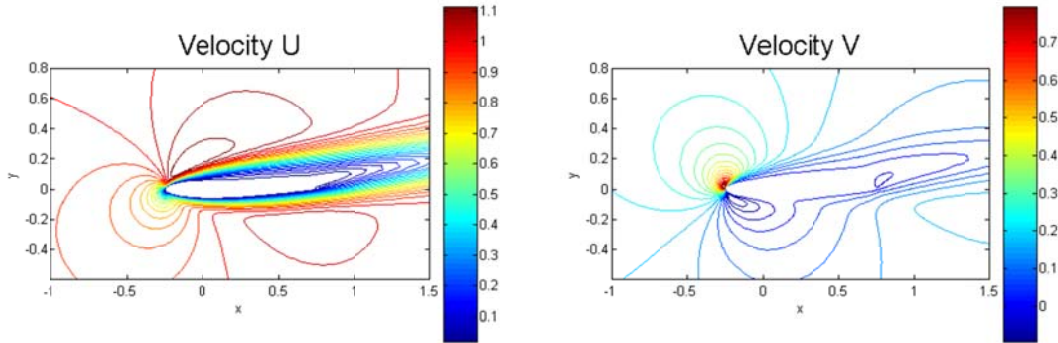

Figure 12. Velocity contours for an airfoil NACA 0012
at $\mathbf{10°}$ angle of attack and $\boldsymbol{Re = 500}$.

The results for an angle of attack of 10° are presented below. The contours for velocity, pressure and vorticity are shown in in Figure 12 and Figure 13. The dimensionless surface pressure coefficient is plotted together with results from [15] and [16] in Figure 14. All the results are in very good agreement with the literature sources.
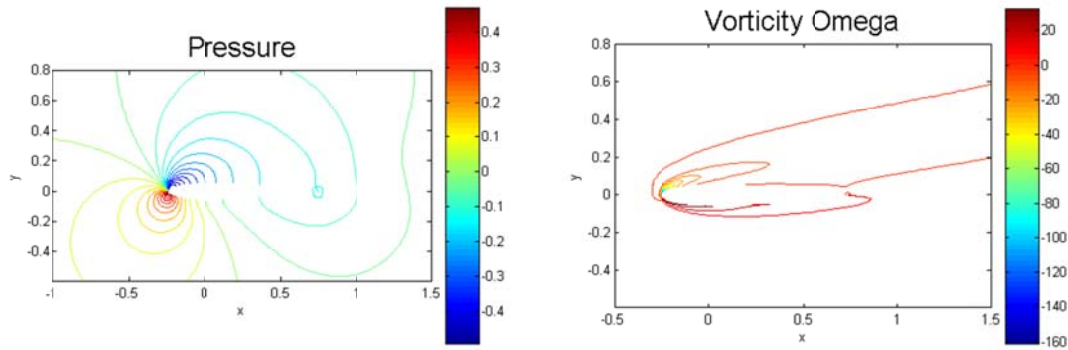
Figure 13. Pressure and vorticity contours for an airfoil NACA 0012
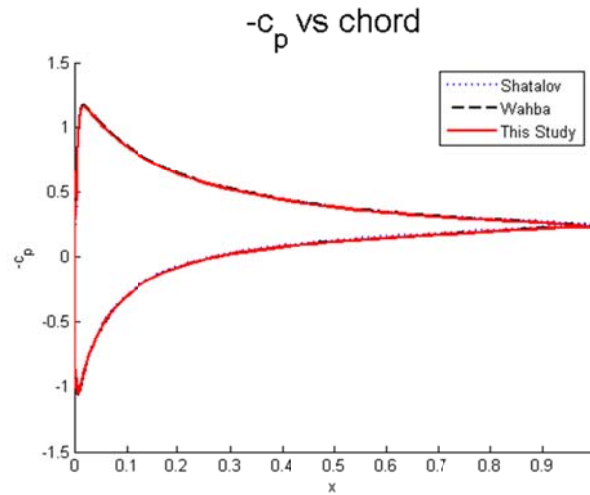at $10°$ angle of attack and $Re = 500$.

Figure 14. Surface pressure for an airfoil NACA 0012
at $10°$ angle of attack and $Re = 500$.

4. Concluding Remarks

The present formulation is applied to several flow problems and proves to be a promising technique for numerical simulations of incompressible flow, thanks to the use of an efficient direct solver. In most cases convergence to machine accuracy is achieved in a few dozen iterations and requiring usually 10 to 30 seconds of compute time in a standard PC architecture. It was verified that the mass and vorticity definitions are satisfied to round-off error and that the accuracy of the method depends only on the grid. Boundary singularities that lead to numerical chessboard pattern solutions are eliminated by use of the radial interpolation scheme. Extensions to unsteady and compressible flow with third order accuracy will be presented in an upcoming publication.

References

[1] D. Kwak and C. Kiris, Computation of Viscous Incompressible Flows, Springer, 2010.

[2] H. Fasel, "Investigation of the stability of boundary layers by a finite-difference model of the Navier-Stokes equations," *J. Fluid Mech.,* vol. 78, no. 2, pp. 355-383, 1976.

[3] M. Hafez and M. Soliman, "A Velocity Decomposition Method for Viscous Incompressible Flow Calculations, Part II," in *AIAA 9th Comp. Fluid Dyn. Conf*, Buffalo, NY, 1989.

[4] C. Tang and M. Hafez, "Numerical simulation of steady compressible flows using a zonal formulation, Part II: Viscous Flows," *Comp & Fluids,* vol. 30, no. 7-8, pp. 1003-1016, 2001.

[5] G. Fernandez and M. Hafez, "Stable finite-element solution of the incompressible Navier-Stokes equations using linear interpolation for velocity and pressure," *Comp. Methods in App. Mech. & Eng.,* vol. 191, no. 617, pp. 545-559, 2001.

[6] O. Schenk, M. Bollhoefer and R. Roemer, "On large-scale diagonalization techniques for the Anderson model of localization," *SIAM Review,* vol. 50, pp. 91-112, 2008.

[7] O. Schenk, A. Waechter and M. Hagemann, "Matching-based Preprocessing Algorithms to the Solution of Saddle-Point Problems in Large-Scale Nonconvex Interior-Point Optimization," *J. Comp. Optimization and Applications,* vol. 36, no. 2-3, pp. 321-341, 2007.

[8] N. I. M. Gould, Y. Hu and J. A. Scott, A numerical evaluation of sparse direct solvers for the solutions of large sparse, symmetric linear systems of equations, Council for te Central Laboratory of Research Councils: RAL-TR-2005-005, 2005.

[9] B. Chacon, Numerical simulation using a Velocity-Pressure-Vorticity formulation, UC Davis: Ph.D. disertation, 2012.

[10] S. C. R. Dennis and G.-Z. Chang, "Numerical solutions for steady flow past a circular cylinder at Reynolds numbers up to 100," *J. Fluid Mech.,* no. 42, pp. 471-489, 1970.

[11] H. Takami and H. B. Keller, "Steady two-dimensional viscous flow of an incompressible fluid past a circular cylinder," *Phys. Fluids, Suppl. II,* no. 12, pp. 51-56, 1969.

[12] S. Tanaeda, "Experimental investigation of the wakes behind cylinders and plates at low Reynolds numbers," *J. Phys. Soc. Japan,* vol. 11, no. 3, pp. 302-307, 1956.

[13] D. Stojkovic, M. Breuer and F. Durst, "Effect of high rotation rates on the laminar flow around a circular cylinder," *Phys. Fluids,* no. 14, pp. 3160-3178, 2002.

[14] H. M. Badr, S. C. R. Dennis and P. J. S. Young, "Steady and unsteady flow past a rotating circular cylinder at low Reynolds number," *Comp. & Fluids,* no. 17, pp. 579-607, 1989.

[15] M. Hafez, A. Shatalov and E. Wahba, "Numerical Simulations of Incompressible aerodynamic flows using viscous/inviscid interaction procedures," *Comp. Methods in App. Mech.& Eng.,* no. 195, pp. 3110-3127, 2006.

[16] M. Hafez and E. Wahba, "Numerical Simulations of transonic aerodynamic flows based on a hierarchical formulation," *J. Num. Methods in Fluids,* vol. 57, no. 6-7, pp. 491-516, 2005.